*energies*

*Article*

# Artificial Neural Networks as a Tool for High-Accuracy Prediction of In-Cylinder Pressure and Equivalent Flame Radius in Hydrogen-Fueled Internal Combustion Engines

**Federico Ricci *, Massimiliano Avana and Francesco Mariani**

Department of Engineering, University of Perugia, Via G. Duranti 93, 06125 Perugia, Italy; massimiliano.avana@unipg.it (M.A.); francesco.mariani@unipg.it (F.M.)
* Correspondence: federico.ricci@unipg.it

**Abstract:** The automotive industry is under increasing pressure to develop cleaner and more efficient technologies in response to stringent emission regulations. Hydrogen-powered internal combustion engines represent a promising alternative, offering the potential to reduce carbon-based emissions while improving efficiency. However, the accurate estimation of in-cylinder pressure is crucial for optimizing the performance and emissions of these engines. While traditional simulation tools such as GT-POWER are widely utilized for these purposes, recent advancements in artificial intelligence provide new opportunities for achieving faster and more accurate predictions. This study presents a comparative evaluation of the predictive capabilities of GT-POWER and an artificial neural network model in estimating in-cylinder pressure, with a particular focus on improvements in computational efficiency. Additionally, the artificial neural network is employed to predict the equivalent flame radius, thereby obviating the need for repeated tests using dedicated high-speed cameras in optical access research engines, due to the resource-intensive nature of data acquisition and post-processing. Experiments were conducted on a single-cylinder research engine operating at low-speed and low-load conditions, across three distinct relative air–fuel ratio values with a range of ignition timing settings applied for each air excess coefficient. The findings demonstrate that the artificial neural network model surpasses GT-POWER in predicting in-cylinder pressure with higher accuracy, achieving an RMSE consistently below 0.44% across various conditions. In comparison, GT-POWER exhibits an RMSE ranging from 0.92% to 1.57%. Additionally, the neural network effectively estimates the equivalent flame radius, maintaining an RMSE of less than 3%, ranging from 2.21% to 2.90%. This underscores the potential of artificial neural network-based approaches to not only significantly reduce computational time but also enhance predictive precision. Furthermore, this methodology could subsequently be applied to conventional road engines exhibiting characteristics and performance similar to those of a specific optical engine used as the basis for the machine learning analysis, offering a practical advantage in real-time diagnostics.

**Keywords:** hydrogen fuel; internal combustion engine; SI engine; ultra-lean conditions; GT-POWER; 1D software; optical access engine; high speed camera; combustion images; artificial intelligence; artificial neural networks; machine learning

check for updates

Academic Editor: Felix Barreras

Received: 12 December 2024
Revised: 7 January 2025
Accepted: 9 January 2025
Published: 11 January 2025

**Citation:** Ricci, F.; Avana, M.; Mariani, F. Artificial Neural Networks as a Tool for High-Accuracy Prediction of In-Cylinder Pressure and Equivalent Flame Radius in Hydrogen-Fueled Internal Combustion Engines. *Energies* **2025**, *18*, 299. https://doi.org/10.3390/en18020299

**Copyright:** © 2025 by the authors. Licensee MDPI, Basel, Switzerland. This article is an open access article distributed under the terms and conditions of the Creative Commons Attribution (CC BY) license (https://creativecommons.org/licenses/by/4.0/).

## 1. Introduction

In response to intensifying environmental regulations aimed at reducing greenhouse gases (GHG) and air pollutants [1,2], the automotive industry is under growing pressure

to develop advanced technologies that lower emissions while maintaining high performance [3,4]. Nowadays, traditional spark ignition (SI) engines struggle to balance high performance with low emissions [5,6]. Among the various strategies pursued, including hybrid and electric vehicles [7,8] and the utilization of alternative and renewable fuels [9,10] such as methanol M100 [11], ethanol E85 [12], etc., hydrogen ($H_2$)-powered internal combustion engines (ICEs) have emerged as a viable alternative to traditional fossil-fuel-based engines [13,14].

Hydrogen presents distinct advantages as a fuel, notably its high flame propagation speed and broad flammability limits [15,16]. These characteristics enable the extension of the lean stable limit of the engine [17,18], thereby achieving the complete elimination of carbon-based emissions [19,20]. This makes it an attractive candidate for enhancing the efficiency and sustainability of combustion engines, aligning with the industry's shift towards cleaner, greener propulsion systems [21,22]. However, the intrinsic characteristics of hydrogen combustion introduce complexities in engine calibration [23], necessitating precise control over combustion dynamics to avoid issues such as backfire [24], misfires [25], delayed combustion [26], knocking [27] and increased pollutant emissions [28], in particular nitrogen oxide ($NO_x$) formation. Accurate estimation of in-cylinder pressure is thus essential for optimizing the performance, efficiency, and emissions of hydrogen-fueled engines [19,29].

Classic mathematical models for predicting in-cylinder pressure are grounded in thermodynamic principles, primarily the first law of thermodynamics, which relates the change in internal energy to the heat released and work carried out by the system. These models, such as the single-zone and two-zone models, assume simplified combustion chamber dynamics. For instance, the single-zone model treats the cylinder as a homogeneous system, while the two-zone model divides it into burned and unburned gas regions to capture combustion progress. While computationally efficient and suitable for providing insights into general combustion trends, these models are constrained by assumptions like uniform pressure distribution and idealized heat transfer, which can lead to significant inaccuracies under highly transient conditions or in engines with advanced combustion strategies [30]. Contemporary approaches have moved towards integrating computational fluid dynamics (CFD) to account for multi-dimensional effects such as turbulence, stratified fuel-air mixing, and detailed chemical kinetics. These methods significantly improve the accuracy of in-cylinder pressure predictions, particularly under complex operating conditions. For example, fuel composition, air–fuel ratio, and combustion efficiency are explicitly modeled to reflect their influence on heat release rates and peak pressures. However, the increased accuracy comes at the expense of computational cost, making CFD less practical for real-time applications such as onboard engine diagnostics or rapid calibration. Both classic and contemporary models face certain limitations [31]. Key challenges include uncertainties in accurately determining input parameters, such as exact fuel composition or combustion efficiency, as well as difficulties in modeling wall heat transfer and crevice effects [32]. Additionally, the computational demands of high-fidelity models like CFD contrast sharply with the need for faster, real-time solutions in practical engine control applications [33]. Traditionally, 1D simulation tools like GT-POWER have been extensively utilized for this purpose, offering robust capabilities to model and predict in-cylinder phenomena across various engine operating conditions [34,35]. Despite their effectiveness, these tools demand significant computational resources, resulting in extended processing times and elevated costs, particularly as the complexity of modern engines continues to increase [36,37].

Recent advances in artificial intelligence (AI) and machine learning (ML) technologies, specifically the application of artificial neural networks (ANNs), present an innovative approach to addressing these challenges by providing faster, potentially more accurate

predictions of in-cylinder pressure [38,39]. Unlike conventional simulation methods, ANNs have demonstrated the ability to adaptively learn from complex datasets, making them suitable for high-speed, real-time applications. By offering reliable predictions of in-cylinder pressure, ANNs can facilitate the calibration and optimization of hydrogen-powered ICEs under a range of operating conditions, resulting in enhanced efficiency and reduced emissions [40,41]. Consequently, preliminary examinations on dedicated test benches are essential for accurate engine calibration.

Solmaz et al. [42] applied ML to predict in-cylinder pressure in an SI engine using fuzzy logic (FL) and ANN based on experimental data. The SI engine operated at a stoichiometric air–fuel ratio ($\lambda$ = 1.0) across engine speeds of 1200, 1400, and 1600 rpm, with six ignition timings (IT) from 15 to 45 crank angle degrees (CADs). ANN predictions yielded high correlation ($R^2 > 0.995$) with experimental data, outperforming FL, which achieved $R^2$ values between 0.820 and 0.949. The trained ANN model was then used to predict in-cylinder pressure and indicate the mean effective pressure (IMEP) in untested conditions, closely matching experimental IMEP values. The model also accurately identified the ignition timing for maximum brake torque (MBT), supporting its application for engine optimization. Bizon et al. [43] conducted a study on designing and optimizing robust ANNs as virtual sensors for diagnosing a three-cylinder diesel engine under various operating conditions. They employed a feed-forward neural network (FFNN) based on radial basis functions (RBFs) and investigated different radial basis functions and their parameters to enhance accuracy. Validation with external data showed a strong correlation between measured and reconstructed pressure signals. The accuracy of the predicted pressure signals was assessed through mean square error and several derived parameters. The results demonstrated promising performance, indicating the potential use of the FFNNs in closed-loop engine control systems. Murugesan et al. [44] examined the application of artificial intelligence to enhance engine testing efficiency by predicting in-cylinder pressure in a diesel engine based on crank angle and load. They developed an ANN model in MATLAB, trained on data from a single-cylinder diesel engine. Using a back propagation algorithm, the model achieved a mean square error of 0.0012 and a correlation factor of about 0.9999 for training, testing, and validation. The results demonstrated that the ANN model accurately predicted outputs, making it suitable for any single-cylinder diesel engine. This model aims to reduce the time and cost of engine development by minimizing the need for repeated testing.

*Present Contribution*

This research explores the integration of advanced predictive models within the engine control unit (ECU) to facilitate onboard real-time diagnostics, thereby enhancing the efficiency of engine performance monitoring and certification processes. The goal is to eliminate reliance on cumbersome portable devices, enabling the continuous assessment of engine parameters. The study focuses on a comparative analysis of the predictive capabilities of GT-POWER and an ANN model specifically for estimating in-cylinder pressure. Emphasis is placed on the potential improvements in computational efficiency offered by the ANN model. Furthermore, the ANN is applied to predict the equivalent flame radius, which may obviate the need for optical high-speed cameras and facilitate analysis in engines lacking optical access, thus reducing the equipment requirements and costs and broadening the applicability of combustion diagnostics in various engine configurations.

Tests were conducted on a single-cylinder SI research engine fueled with hydrogen ($H_2$), operating under low-speed conditions and low load. The study considered three different relative air excess ratios (i.e., $\lambda$ = 1.6, $\lambda$ = 2.0, $\lambda$ = 2.3) and explored a comprehensive range of operating conditions, with IT varying from $-1$ to $-19$ CAD after top dead center

(aTDC). Additionally, 63 combustion cycles at $\lambda$ = 1.6 and IT = −11 CAD aTDC were recorded using a high-speed camera. The corresponding equivalent flame radius was derived through post-processing analysis of the combustion images.

The research methodology consists of collecting data from ECU, an indicating system and high-speed camera. These data served as training data for the ML architecture, which was developed to forecast the in-cylinder pressure and the equivalent flame radius based on the observed behavior of the engine. To accomplish this mission, different feed-forward neural networks with a back propagation (BP) optimizer [45] were tested. This optimization process involves fine-tuning parameters such as the number of neurons, hidden layers and input variables within ANN structures to enhance predictive performance. Through the iterative execution of experiments and validations, the most effective design of the ANN architecture was identified.

## 2. Materials and Methods

### *2.1. Experimental Setup*

The experiments were performed on a 500-cc single-cylinder optical access engine (Figure 1) featuring a pent-roof combustion chamber, four valves, a quartz crown piston and a reverse-tumble-intake port system designed for port fuel injection (PFI) operation. The optical configuration, composed of a quartz crown piston and a 45-degree mirror, utilizes a mixture of Teflon and graphite for cylinder liner and piston rings, in order to allow dry contact between these components [46,47]. Additional specifications can be found in Table 1.

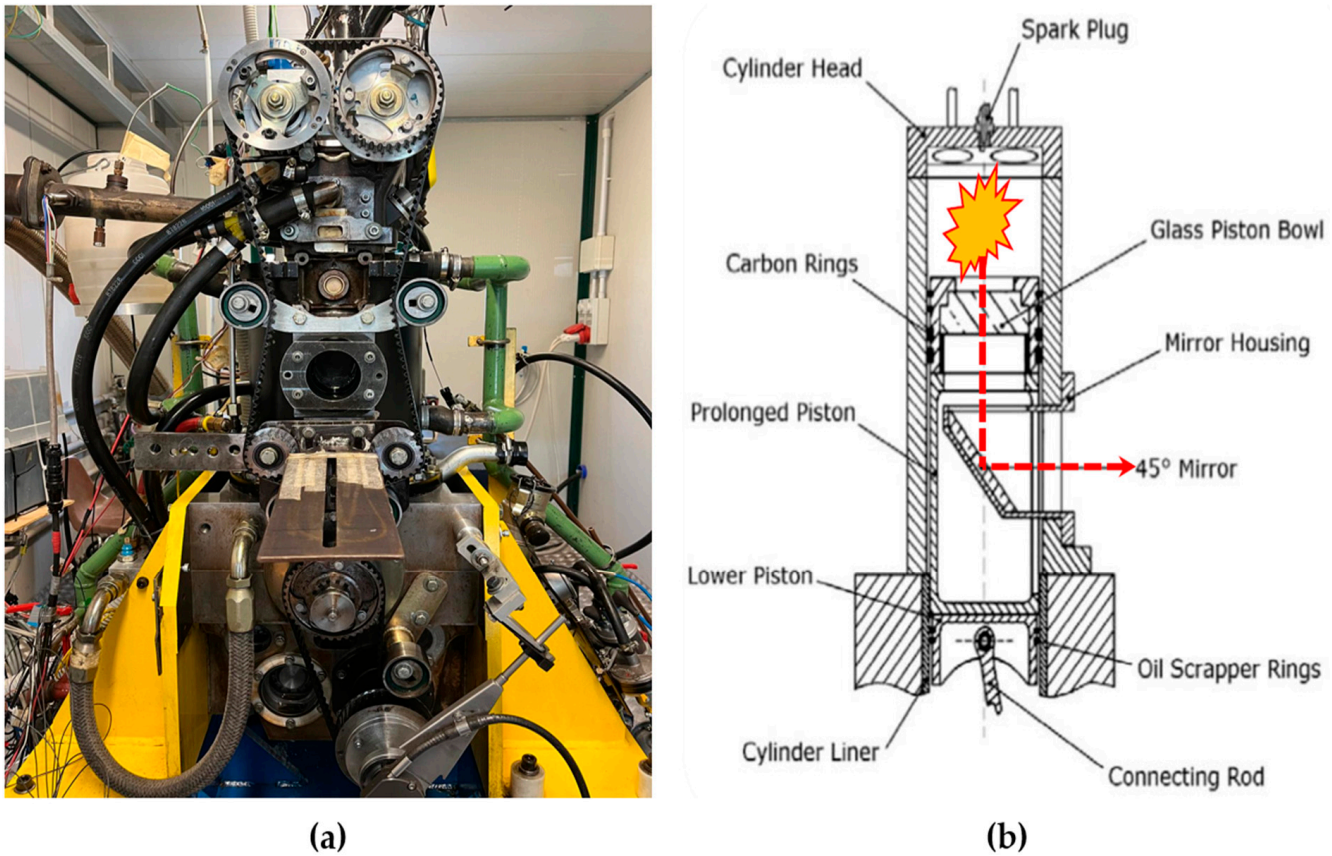



**Figure 1.** Test engine: (**a**) real and (**b**) schematic view.

**Table 1.** Main features of the test engine.

| Feature | Value | Unit |
|---|---|---|
| Displaced volume | 500 | $cm^3$ |
| Stroke | 88 | mm |
| Bore | 85 | mm |
| Connecting rod length | 139 | mm |
| Compression ratio | 8.8:1 | - |
| Number of valves | 4 | - |
| Exhaust valve open | −13 | CAD aBDC |
| Exhaust valve close | 25 | CAD aBDC |
| Intake valve open | −20 | CAD aBDC |
| Intake valve close | −24 | CAD aBDC |

The air-flow rate was fixed using a throttle valve positioned upstream of the intake manifold, while $\lambda$ was regulated by adjusting the injected hydrogen quantity at a constant pressure of 4 bar. The $\lambda$ value was continuously fine-tuned during engine operation to reach the target value by monitoring the $O_2$% concentration. This adjustment follows the method proposed by Azeem et al. [48] (as outlined in Equation (1)):

$$\lambda = \frac{1 + X_{O_2}}{1 - \frac{X_{O_2}}{Y_{O_2}}} \quad (1)$$

In this equation, $X_{O_2}$ and $Y_{O_2}$, defined based on the equation representing the complete combustion of hydrogen and oxygen [48], represent the wet oxygen concentrations in the exhaust gas and air intake (approximately 20.95%), respectively.

A research ECU (Athena GET HPUH4) controlled both the injector energizing time and IT via a trigger signal to the igniter control unit. The experimental setup, including inputs (blue dashed lines) and outputs (red dashed lines) for the AI, is shown in Figure 2, with further details listed in Table 2.

**Table 2.** Test equipment details.

| Device | Description | Specifications |
|---|---|---|
| Kistler Kibox | Indicating combustion analysis system for signal acquisition | 10 analog input channels<br>2 encoder input channels |
| Kistler 6061B | In-cylinder pressure piezoelectric sensor | Sensitivity: 25.9 pC/bar<br>Range: 0–250 bar |
| Kistler 5011B | Charge amplifier | Scale: 10 bar/V |
| Kistler 4075A5 | Intake pressure piezoresistive sensor, downstream of throttle; reference for in-cylinder pressure pegging | Sensitivity: 25 mV/bar/mA<br>Range: 0–5 bar |
| AVL 365C | Optical encoder for crankshaft angular position and engine speed measurement | Resolution up to 0.1 CAD |
| AVL 5700 | Dynamic brake, mechanically coupled with the engine crankshaft | Ensures the engine speed control through National Instruments hardware and in-house LabVIEW code |
| Athena GET HPUH4 | Engine control unit | Controls the injector energizing time and IT by sending a trigger signal to the igniter control unit |
| Horiba Mexa 720 | Fast lambda probe | Output: AFR, $\lambda$ and $O_2$%; can be used for different fuels via O/C and H/C ratio setting<br>Accuracy: ±0.5% |
| VEO-E Phantom 310-L | High-speed camera | Records the natural luminosity of initial combustion flames |

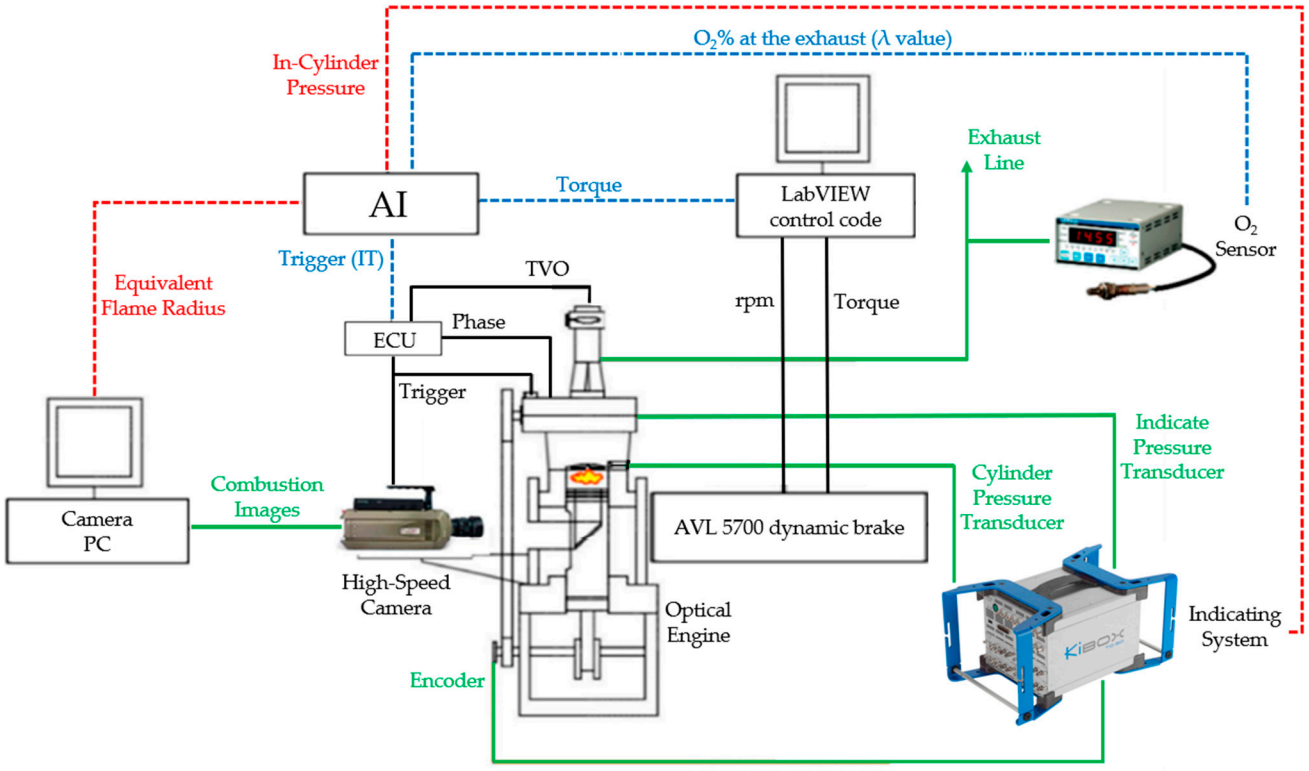



**Figure 2.** Test equipment.

### *2.2. Imaging System Setup*

The natural luminosity of initial combustion flames was recorded using a VEO-E Phantom 310-L high-speed camera, equipped with a Nikon 55 mm f/2.8 lens (Figure 3). Table 3 provides a summary of the principal optical parameters used. For each testing condition, 63 consecutive combustion cycles were recorded. Synchronization with indicator data was achieved through a common trigger, as described in Figure 2, facilitating the alignment of flame development with in-cylinder pressure traces for each individual cycle.




**Figure 3.** VEO-E Phantom 310-L high-speed camera, equipped with a Nikon 55 mm f/2.8 lens.

**Table 3.** Imaging setup specifications.

| Feature | Value | Unit |
|---|---|---|
| Image resolution | 512 × 512 | pixel |
| Sampling rate | 11 | kHz |
| Exposure time | 90 | µs |
| Bit depth | 8 | bit |
| Spatial resolution | 130 | µm/pixel |
| Temporal resolution (at 1000 rpm) | 0.6 | CAD/frame |
| N° of events recorded | 63 | - |

This configuration enabled a detailed analysis of early flame development. The temporal resolution, on the order of 0.55 CAD per frame, allowed for the capture of the sequence of combustion onset images for each cycle. Due to the effects of flame wrinkling, distortion, and convection, the maximum detectable average flame radius within the optical boundaries was approximately 20 mm, which corresponded to roughly 5% of the mass fraction burned (MFB) [49], as indicated by the indicating system through the AI05 value, the CAD aTDC at which 5% of the mass is burned. Consequently, high-speed imaging offered valuable two-dimensional information on early flame development (within a swirl plane), complementing the data acquired by the indicating system.

A dedicated in-house MATLAB algorithm was employed to extract quantitative information from the grayscale combustion images [50]. For each combustion event, following the processes of filtering and ignition detection, the algorithm applied a thresholding technique based on the semi-automatic method outlined by Shawal et al. [51]. Once binarized, the algorithm computed essential metrics, such as the equivalent flame radius over time (along with its average across consecutive combustion events) and the average flame growth rate in the swirl plane (i.e., the time derivative of the average radius). Additionally, the algorithm provided information regarding temporal and spatial repeatability, with the latter assessed based on flame probability presence, consistent with the method proposed by Aleiferis et al. [52].

Further details concerning the imaging setup and the applied algorithms are available in other publications from our research group [49,50].

### *2.3. GT-POWER Setup*

GT-POWER [53,54] is a 1D engine-modeling and simulation tool used during engine development. It provides predictive simulations for combustion, including turbulence and knock predictions, and thermodynamic simulations involving cylinders, valves, and interactions with the engine body, coolant, and environment. The tool models fluid dynamics from intake to exhaust, accounting for engine geometry, pressure drops, and after-treatment components. It also simulates mechanical loads, friction, lubrication, and sonic/subsonic behavior in valves and turbochargers. GT-POWER offers physical torque data and can integrate with electrical motors, transmissions, and vehicle-level after-treatment systems.

In this study, a GT-POWER model (GT-POWER version number: GT-ISE v2022) was developed to simulate the operation of the engine described in the preceding paragraph, with the primary aim of determining the in-cylinder pressure. As depicted in Figure 4, a digital single-cylinder engine is developed, where hydrogen is injected in the intake manifold in front of the intake splitter and then mixed with air that subsequently flows through two intake valves into the engine cylinder. To calibrate the predictive combustion model, it is essential to have experimental data, including in-cylinder pressure profiles and IMEP values [34,55]. The validation of the GT-POWER model in relation to the experimental data is presented in Figure 5.

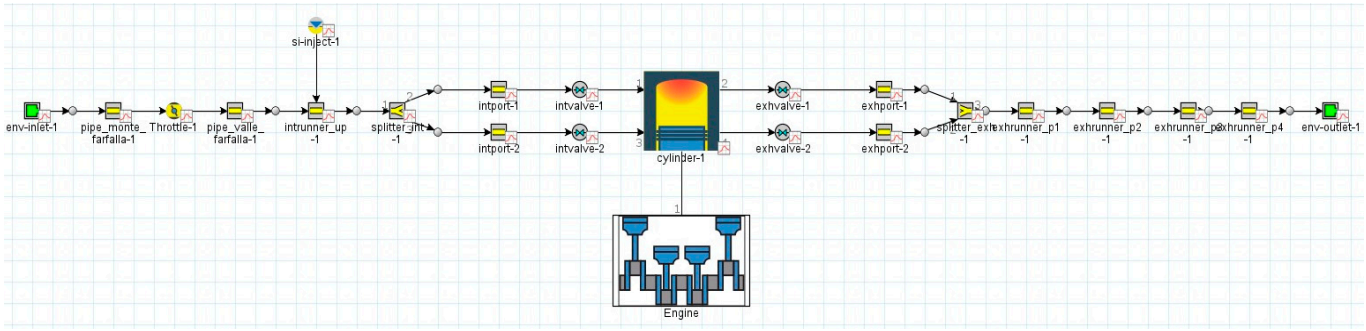



**Figure 4.** GT-POWER engine model configuration.

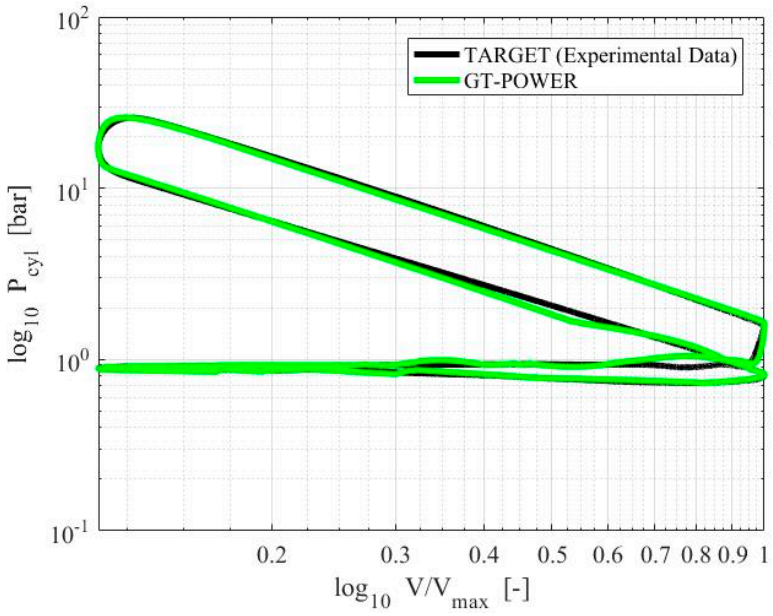



**Figure 5.** GT-POWER engine model validation: logP-logV curves for numerical (green) and experimental (black) data at $\lambda$ = 2.0 and IT = −13 CAD aTDC.

The model was constructed by incorporating several critical parameters, listed in Table 4, including the lambda value, which directly influences the air–fuel ratio and injector delivery rate; the type of fuel utilized; and the geometrical specifications of the cylinder, piston, and valves, as well as the intake and exhaust ports. Furthermore, the fluid conditions prior to and following combustion (including pressure, temperature, and composition) were meticulously defined, along with the relevant boundary conditions.

**Table 4.** Model's intake and exhaust conditions and injection conditions.

| Feature | Value | Unit |
|---|---|---|
| Intake pressure | 1 | bar |
| Intake temperature | 310 | K |
| Intake fluid composition | air | - |
| Exhaust pressure | 1 | bar |
| Exhaust temperature | 1130 | K |
| Exhaust fluid composition | exhaust gases | - |
| Injector delivery rate | 0.0360 ($\lambda$ = 1.6)<br>0.0326 ($\lambda$ = 2.0)<br>0.0303 ($\lambda$ = 2.3) | g/s |
| Injected fuel temperature | 293 | K |
| Injection timing angle | 360 | deg |
| Injection location | outlet end of the pipe (1.0) | - |

This comprehensive parameterization ensures that the model accurately reflects the engine's real-world performance characteristics.

### *2.4. Artificial Neural Network Setup*

For this study, a Back-Propagation Artificial Neural Network (BPANN) was selected as the artificial neural network [56]. BPANN is a type of ANN widely used in supervised learning operations. It is structured to learn from input data by minimizing the error between its predictions and the actual outcomes through a method called back-propagation. The network, shown in Figure 6, is organized into layers: an input layer for receiving raw data, one or more hidden layers for processing the data, and an output layer for producing predictions. Neurons in these layers multiply inputs by weights, apply activation functions like Sigmoid or ReLU to introduce non-linearity, and pass results to the next layer [57].

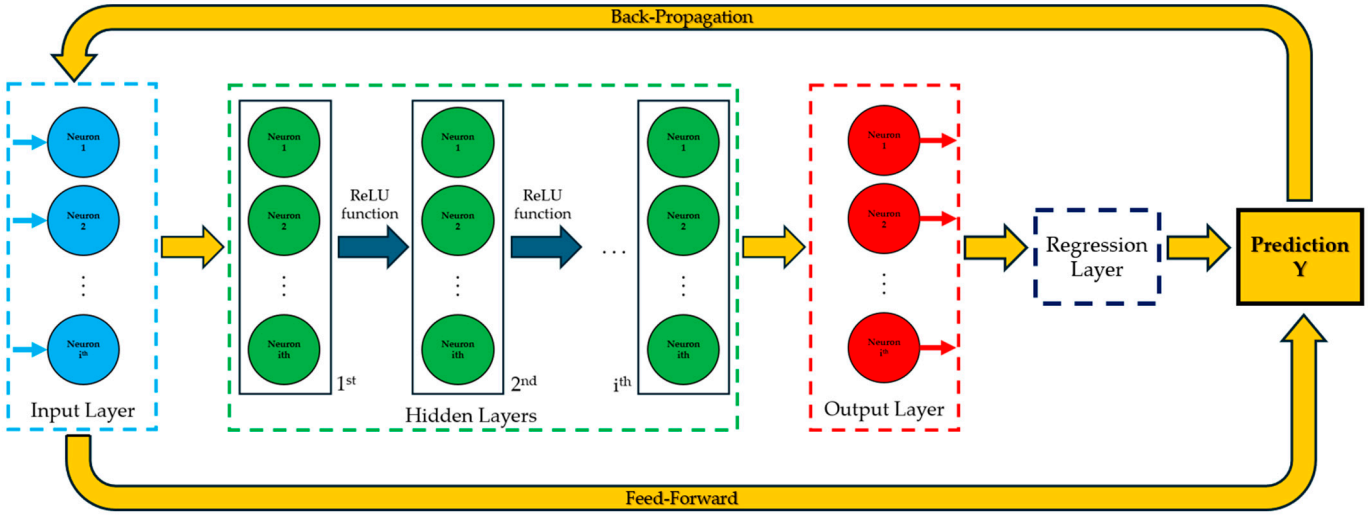



**Figure 6.** Conceptual layout of the BPANN [54].

In a forward pass, data flow through each layer to generate an output based on hidden layer processing. This output is then compared to the actual target using a loss function to measure prediction error. Back-propagation then transmits this error backward from the output to the input layer. By calculating gradients of the loss with respect to each weight, the network updates weights in a way that reduces error, often using optimization methods such as gradient descent [45].

This iterative process, in which each iteration is referred to as an epoch, enables the network to incrementally adjust its weights, minimizing error and thereby enhancing its performance on the training data. Critical concepts in this process include the learning rate, which determines the speed of learning adjustments; overfitting, a phenomenon whereby the network performs well on training data but poorly on new, unseen data, often addressed through regularization techniques; and convergence, the point at which training stabilizes as the network approaches optimal weights.

An initial comparative analysis of BP neural architectures was performed, emphasizing the optimization of their internal configurations to enhance prediction accuracy and accelerate convergence rates. This optimization process included testing different quantities of hidden layers, neurons, and activation functions. All tasks, encompassing the development and optimization of the architecture, were carried out within the MATLAB environment (MATLAB version number: MATLAB R2024a), utilizing a single Central Processing Unit (CPU) and 16 GB of Random Access Memory (RAM).

To evaluate the accuracy and efficacy of the model's parameters, the RMSE was used as the primary metric for assessing loss. This metric represents the average of the

squared differences between predicted and observed normalized values (as outlined in Equation (2)).

$$\text{RMSE } [\%] = 100 \times \sqrt{\frac{1}{N}\sum_{i=1}^{N}\left(Y^{i}_{predicted,N} - Y^{i}_{target,N}\right)^{2}} \quad (2)$$

where

- $N$ = number of observations.
- $i = i^{\text{th}}$ temporal instant.
- $Y^{i}_{predicted,\,N}$ = normalized predicted value.
- $Y^{i}_{target,\,N}$ = normalized target value (experimental results).

In such analysis, it is standard practice to utilize supplementary metrics to further assess the performance of the model, including the mean squared error (MSE), the mean absolute error (MAE), and, as in this specific study, the percentage error (ERR), defined as the distance between the approximate value and the exact value as a percentage of the actual value (as outlined in Equation (3)).

$$\text{ERR } [\%] = 100 \times \frac{1}{N}\sum_{i=1}^{N}\frac{\left|Y^{i}_{predicted} - Y^{i}_{target}\right|}{Y^{i}_{target}} \quad (3)$$

where

- $Y^{i}_{predicted}$ = predicted value (not normalized).
- $Y^{i}_{target}$ = target value (not normalized).

To ensure optimal prediction accuracy, an upper limit of 10% has been set for both the RMSE and the ERR [40,58]. To optimize BPANN architecture, the structural parameters considered include the number of hidden layers (ranging from 2 to 6) and neurons per layer (from 20 to 100). Training was conducted over 10,000 epochs, allowing final loss values to be calculated upon reaching maximum iterations.

The optimal BPANN configuration has an input layer of three neurons, corresponding to input variables, followed by four hidden layers with 100 neurons each, separated by ReLU activation functions to enhance the recognition of complex, non-linear patterns. The output layer contains two neurons, matched to the input variables purely by coincidence rather than design constraints.

This configuration, fine-tuned through initial analysis, leverages deep learning with multiple hidden layers and ReLU activations for improved pattern recognition and prediction. The Adam optimizer, used here, applies an adaptive learning rate and momentum adjustments, which effectively streamline weight and bias adjustments, boosting the model's performance and convergence speed.

## 3. Description of the Datasets

This study assesses the effectiveness of a backpropagation neural network architecture in predicting in-cylinder pressure ($P_{cyl}$) and estimating the equivalent flame radius ($r_{eq}$), utilizing three distinct datasets, each tailored to a specific predictive task. The analysis aims to rigorously evaluate the network's performance across these separate datasets, providing insights into the model's adaptability and accuracy for different combustion-related predictions.

### *3.1. Dataset 1*

The initial dataset employed in this study consists of experimental data gathered under three different values of $\lambda$ (specifically, $\lambda$ = 1.6, $\lambda$ = 2.0, and $\lambda$ = 2.3), while maintaining a

constant TVO value (10%) and engine speed (1000 rpm). Figure 7 provides an overview of the structure and characteristics of Dataset 1.

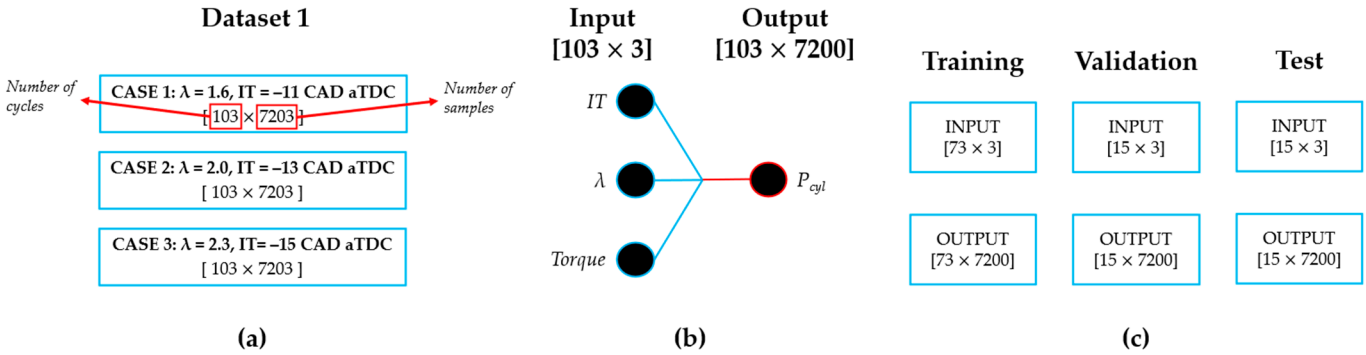



**Figure 7.** (**a**) Dataset 1 structure; (**b**) input–output structure of the BPANN model; (**c**) data partitioning.

Figure 7a illustrates the structure of Dataset 1, comprising three distinct cases. Each case is characterized by specific parameter values. CASE 1 has $\lambda$ = 1.6 and an IT of −11 CAD aTDC, CASE 2 has $\lambda$ = 2.0 and IT = −13 CAD aTDC, and CASE 3 has $\lambda$ = 2.3 and IT = −15 CAD aTDC. For all cases, the data matrix has a size of [103 × 7203], where 103 represents the number of cycles and 7203 represents the number of samples per combustion cycle.

Figure 7b shows the model's input–output structure. The input to the model has a size of [103 × 3], indicating 103 combustion cycles with three variables: injection timing, $\lambda$, and torque. The output, with a size of [103 × 7200], corresponds to the $P_{cyl}$, across 7200 samples per cycle. The input variables are connected to the output through the BPANN.

Figure 7c illustrates the data partitioning used for model training and evaluation. The data are divided into training, validation, and test subsets. The training set includes 73 cycles, with an input dimension of [73 × 3] and an output dimension of [73 × 7200]. The validation and test sets each consist of 15 combustion cycles per case, characterized by input dimensions of [15 × 3] and output dimensions of [15 × 7200]. This partitioning scheme is designed to support model training and performance assessment.

### *3.2. Dataset 2*

The second dataset employed in this study consists of an experimental data gathered under the same values of $\lambda$, TVO, and engine speed as those in Dataset 1, with IT varying from −1 to −19 CAD aTDC. Figure 8 provides an overview of the structure and characteristics of Dataset 2.

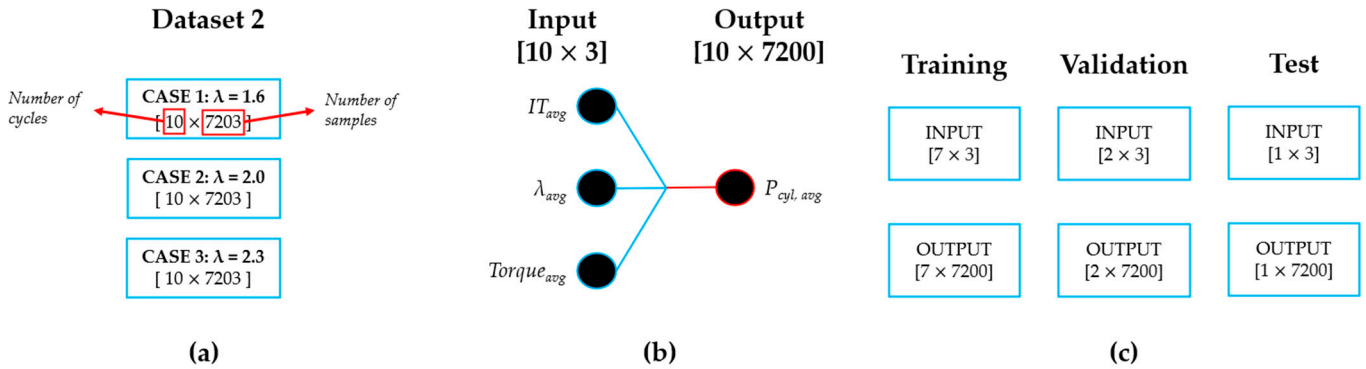



**Figure 8.** (**a**) Dataset 2 structure; (**b**) input–output structure of the BPANN model; (**c**) data partitioning.

Figure 8a illustrates the structure of Dataset 2, which comprises three distinct cases: CASE 1 has $\lambda$ = 1.6, CASE 2 has $\lambda$ = 2.0 and CASE 3 has $\lambda$ = 2.3. For all cases, the data

matrix has a size of [10 × 7203], where 10 represents the number of averaged cycles over 103 individual cycles and 7203 represents the number of samples per cycle.

Figure 8b presents the input–output structure of the model. The input has dimensions of [10 × 3], representing 10 averaged combustion cycles with three variables: mean ignition timing ($IT_{avg}$), mean $\lambda$ ($\lambda_{avg}$), and mean torque ($Torque_{avg}$). The output, with a size of [1 × 7200], corresponds to the average value of the in-cylinder pressure ($P_{cyl,\,avg}$), across 7200 samples per cycle.

Figure 8c depicts the data partitioning utilized for model training and evaluation. The data are divided into training, validation, and test subsets. The training set comprises seven cycles, with an input dimension of [7 × 3] and an output dimension of [7 × 7200]. The validation subset consists of two cycles, characterized by input dimensions of [2 × 3] and output dimensions of [2 × 7200]. In contrast, the test subset includes one specific cycle per CASE, with input dimensions of [1 × 3] and output dimensions of [1 × 7200]. Moreover, each output obtained for each CASE was subsequently compared with the corresponding output generated by GT-POWER.

### *3.3. Dataset 3*

The third dataset comprises 63 experimental cases at $\lambda$ = 1.6 and IT = −11 CAD aTDC, for which the evolution of the flame front was recorded using the high-speed camera detailed in Section 2.2. The corresponding equivalent flame radii, utilized for BPANN training and validation, were derived through post-processing analysis of the combustion images.

Figure 9a illustrates the structure of Dataset 3: the dataset matrix has a size of [63 × 7271], where 63 represents the number combustion cycles recorded and 7271 represents the number of samples per cycle.

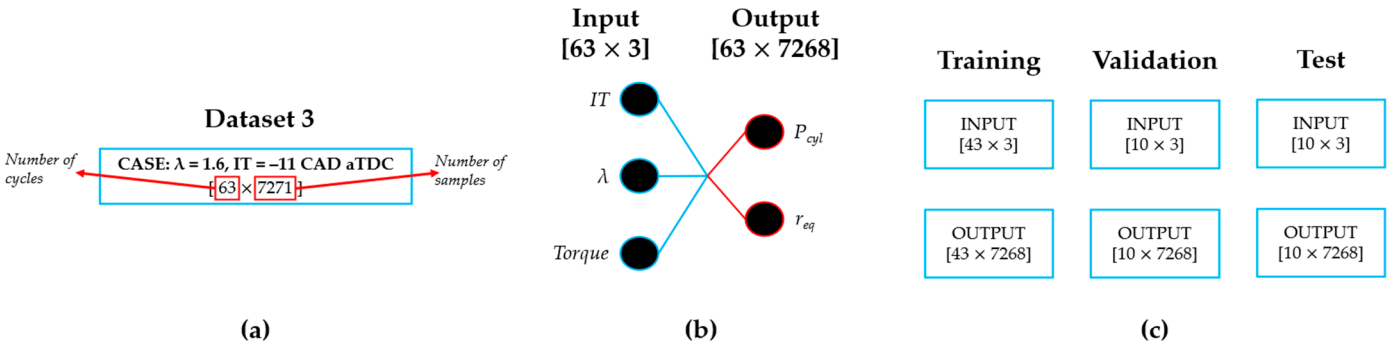



**Figure 9.** (**a**) Dataset 3 structure; (**b**) input–output structure of the BPANN model; (**c**) data partitioning.

Figure 9b presents the model's input–output structure. The input has dimensions of [63 × 3], indicating 63 combustion cycles with three variables: IT, $\lambda$, and torque. The output matrix [63 × 7268] corresponds to the $P_{cyl}$ and the related $r_{eq}$, with sizes of [63 × 7200] and [63 × 68], respectively.

Figure 9c depicts the data partitioning utilized for model training and evaluation. The training set comprises 43 cycles, with an input dimension of [43 × 3] and an output dimension of [43 × 7268]. The validation and test sets each consist of 10 combustion cycles, characterized by input dimensions of [10 × 3] and output dimensions of [10 × 7268].

## 4. Results and Discussion

### *4.1. Dataset 1 Results*

Figures 10–12 provide a detailed comparison of the BPANN model's performance in predicting $P_{cyl}$ across 45 combustion cycles for Dataset 1 (15 cycles for each case, as

specified in Figure 7), with $\lambda$ values of 1.6, 2.0, and 2.3, and IT of −11, −13, and −15 CAD aTDC, respectively. In the figures, predictions (red curves) closely match the target values (black curves), illustrating the model's accuracy under these varying operating conditions. Furthermore, for each cycle, the accuracy of predicting the maximum in-cylinder pressure ($P_{max}$) and the crank angle degree at which $P_{max}$ occurs ($AP_{max}$) was assessed. As demonstrated in Tables 5–7, the values of RMSE $P_{cyl}$, ERR $P_{max}$, and ERR $AP_{max}$ remain significantly below the upper limit of 10% across all cycles. Specifically, for $\lambda$ = 1.6, the average RMSE $P_{cyl}$ is 0.36%, with ERR $P_{max}$ averaging 1.39% and ERR $AP_{max}$ averaging 4.59%. As $\lambda$ increases to 2.0, the average RMSE $P_{cyl}$ increases slightly to 0.41%, while ERR $P_{max}$ and ERR $AP_{max}$ also rise to averages of 1.70% and 4.82%, respectively. At $\lambda$ = 2.3, the average RMSE $P_{cyl}$ further increases to 0.44%, with ERR $P_{max}$ and ERR $AP_{max}$ showing average values of 1.78% and 4.92%, respectively.

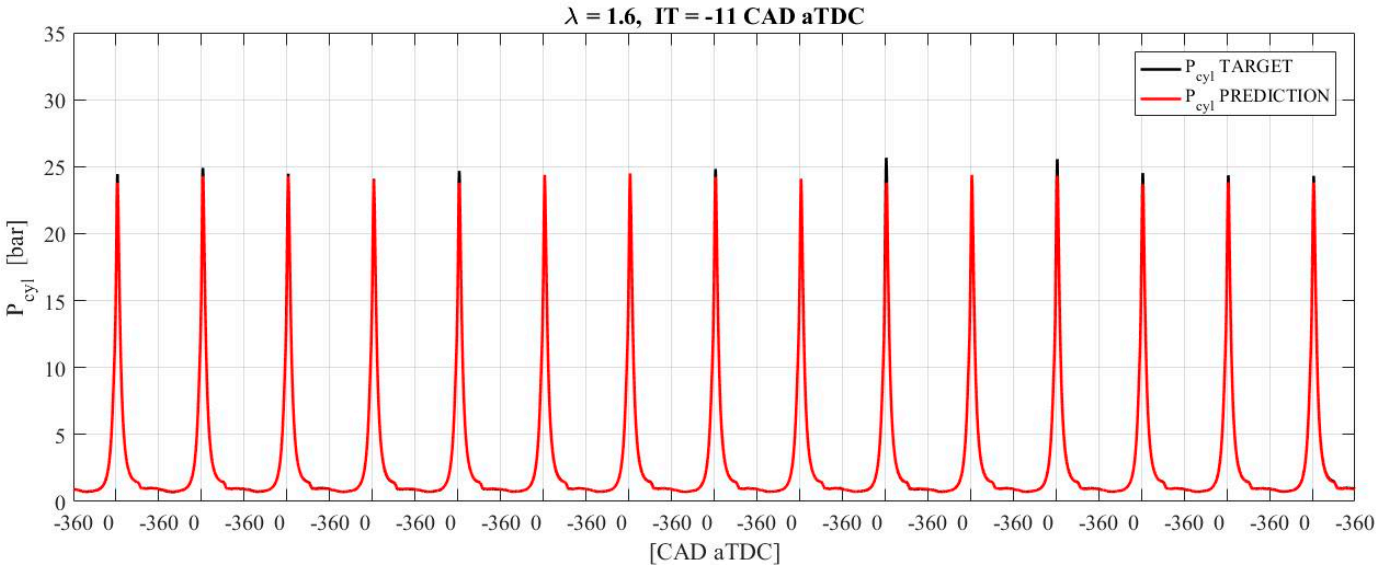



**Figure 10.** BPANN prediction of in-cylinder pressure for $\lambda$ = 1.6 and IT = −11 CAD aTDC.

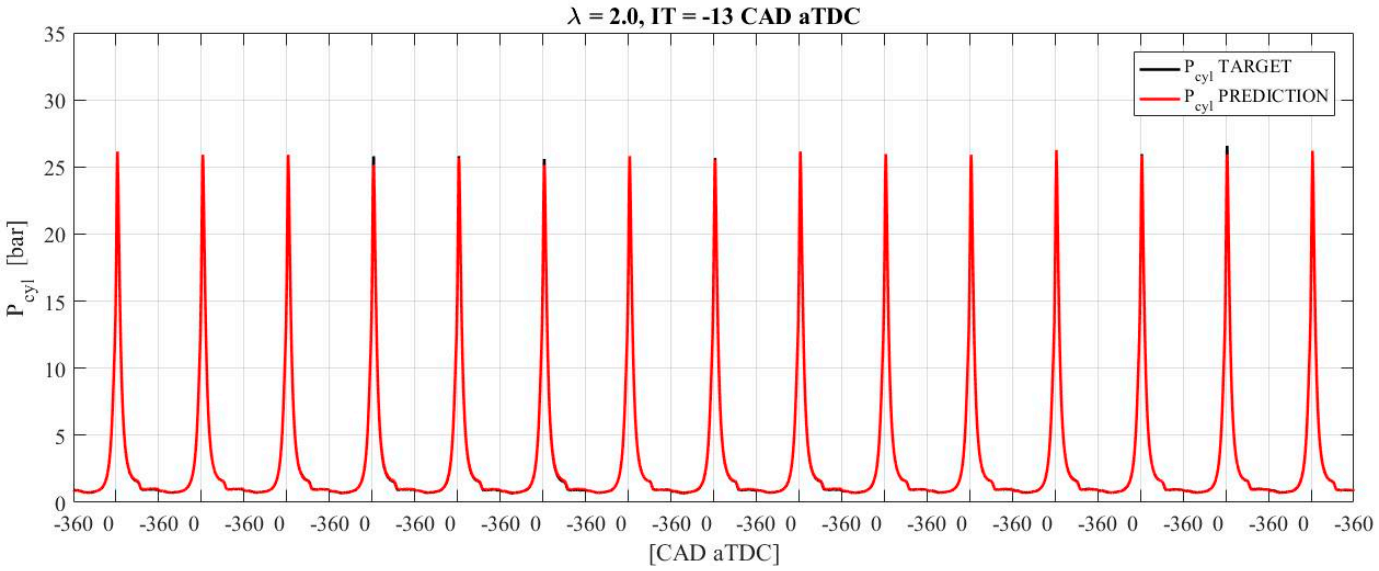



**Figure 11.** BPANN prediction of in-cylinder pressure for $\lambda$ = 2.0 and IT = −13 CAD aTDC.

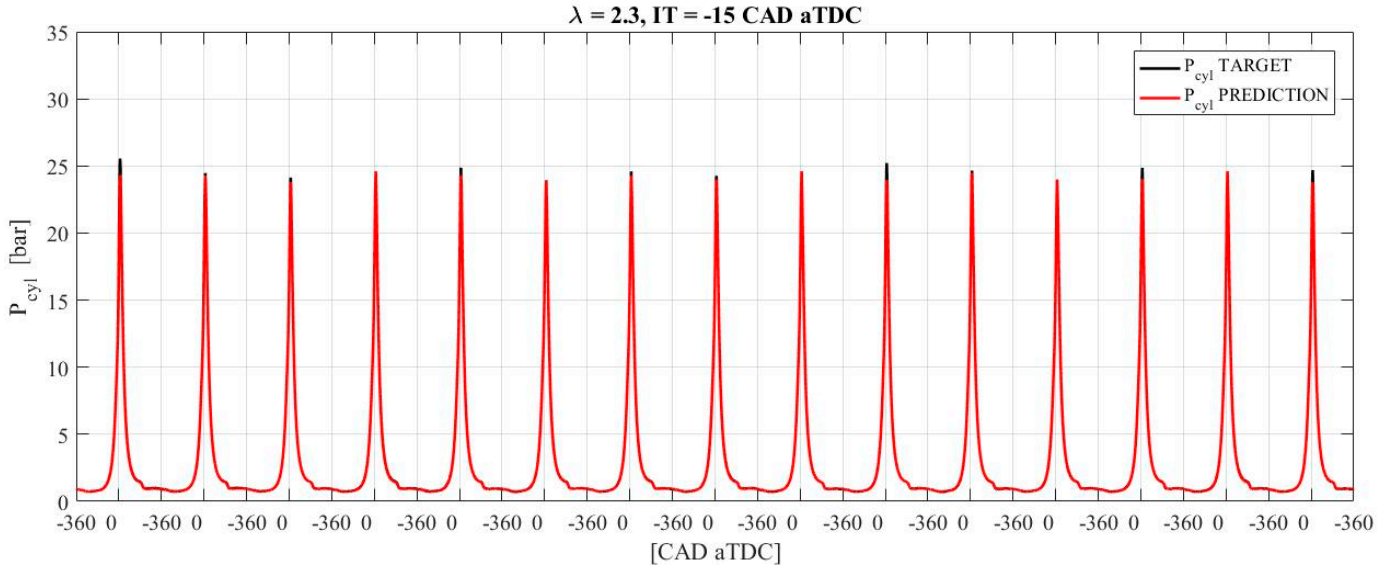



**Figure 12.** BPANN prediction of in-cylinder pressure for $\lambda$ = 2.3 and IT = −15 CAD aTDC.

**Table 5.** Main results for $\lambda$ = 1.6 and IT = −11 CAD aTDC.

| Cycle Number [-] | RMSE $P_{cyl}$ [%] | ERR $P_{max}$ [%] | ERR $AP_{max}$ [%] |
|---|---|---|---|
| 1 | 0.26 | 1.46 | 2.46 |
| 2 | 0.58 | 1.32 | 4.39 |
| 3 | 0.34 | 0.52 | 8.85 |
| 4 | 0.17 | 0.58 | 1.87 |
| 5 | 0.26 | 1.81 | 6.84 |
| 6 | 0.23 | 1.79 | 5.09 |
| 7 | 0.71 | 2.22 | 8.16 |
| 8 | 0.72 | 3.04 | 5.39 |
| 9 | 0.26 | 2.07 | 5.88 |
| 10 | 0.23 | 0.83 | 4.46 |
| 11 | 0.52 | 1.33 | 9.35 |
| 12 | 0.30 | 1.07 | 1.71 |
| 13 | 0.29 | 1.67 | 2.66 |
| 14 | 0.32 | 0.37 | 0.01 |
| 15 | 0.19 | 0.81 | 1.74 |
| **avg.** | 0.36 | 1.39 | 4.59 |

These findings underscore the robustness and reliability of the predictive model across all conditions examined. The slight increase in average values of RMSE $P_{cyl}$, ERR $P_{max}$, and ERR $AP_{max}$ as $\lambda$ increases suggest a potential degradation in predictive performance; however, all values remain well within acceptable bounds.

**Table 6.** Main results for $\lambda$ = 2.0 and IT = −13 CAD aTDC.

| Cycle Number [-] | RMSE $P_{cyl}$ [%] | ERR $P_{max}$ [%] | ERR $AP_{max}$ [%] |
|---|---|---|---|
| 1 | 0.36 | 1.44 | 4.76 |
| 2 | 0.30 | 0.31 | 0.01 |
| 3 | 0.63 | 4.38 | 7.52 |
| 4 | 0.51 | 2.48 | 8.27 |
| 5 | 0.29 | 0.50 | 5.98 |
| 6 | 0.49 | 1.70 | 6.50 |
| 7 | 0.50 | 2.06 | 8.40 |
| 8 | 0.30 | 0.41 | 1.58 |
| 9 | 0.62 | 4.19 | 7.69 |
| 10 | 0.54 | 1.94 | 7.09 |
| 11 | 0.20 | 0.06 | 0.83 |
| 12 | 0.27 | 2.02 | 2.54 |
| 13 | 0.33 | 0.41 | 1.64 |
| 14 | 0.44 | 2.52 | 7.90 |
| 15 | 0.30 | 1.12 | 1.68 |
| **avg.** | 0.41 | 1.70 | 4.82 |

**Table 7.** Main results for $\lambda$ = 2.3 and IT = −15 CAD aTDC.

| Cycle Number [-] | RMSE $P_{cyl}$ [%] | ERR $P_{max}$ [%] | ERR $AP_{max}$ [%] |
|---|---|---|---|
| 1 | 1.05 | 4.78 | 9.17 |
| 2 | 0.69 | 0.78 | 5.26 |
| 3 | 0.26 | 1.33 | 2.42 |
| 4 | 0.31 | 0.38 | 1.71 |
| 5 | 0.37 | 2.17 | 0.83 |
| 6 | 0.25 | 0.26 | 4.51 |
| 7 | 0.25 | 1.22 | 2.56 |
| 8 | 0.27 | 1.16 | 0.84 |
| 9 | 0.22 | 0.48 | 4.96 |
| 10 | 0.81 | 4.97 | 7.02 |
| 11 | 0.25 | 0.64 | 7.32 |
| 12 | 0.23 | 0.12 | 0.81 |
| 13 | 0.71 | 3.30 | 3.31 |
| 14 | 0.50 | 1.50 | 9.45 |
| 15 | 0.50 | 3.61 | 1.64 |
| **avg.** | 0.44 | 1.78 | 4.92 |

### *4.2. Dataset 2 Results*

Figures 13 and 14 and Table 8 present a comparative analysis of the average in-cylinder pressure prediction performance for the BPANN and GT-POWER models across three

distinct cases, with each figure corresponding to a specific $\lambda$ and IT value. Key parameters evaluated include the RMSE of average in-cylinder pressure (RMSE $P_{cyl, avg}$), ERR $P_{max}$, and ERR $AP_{max}$.

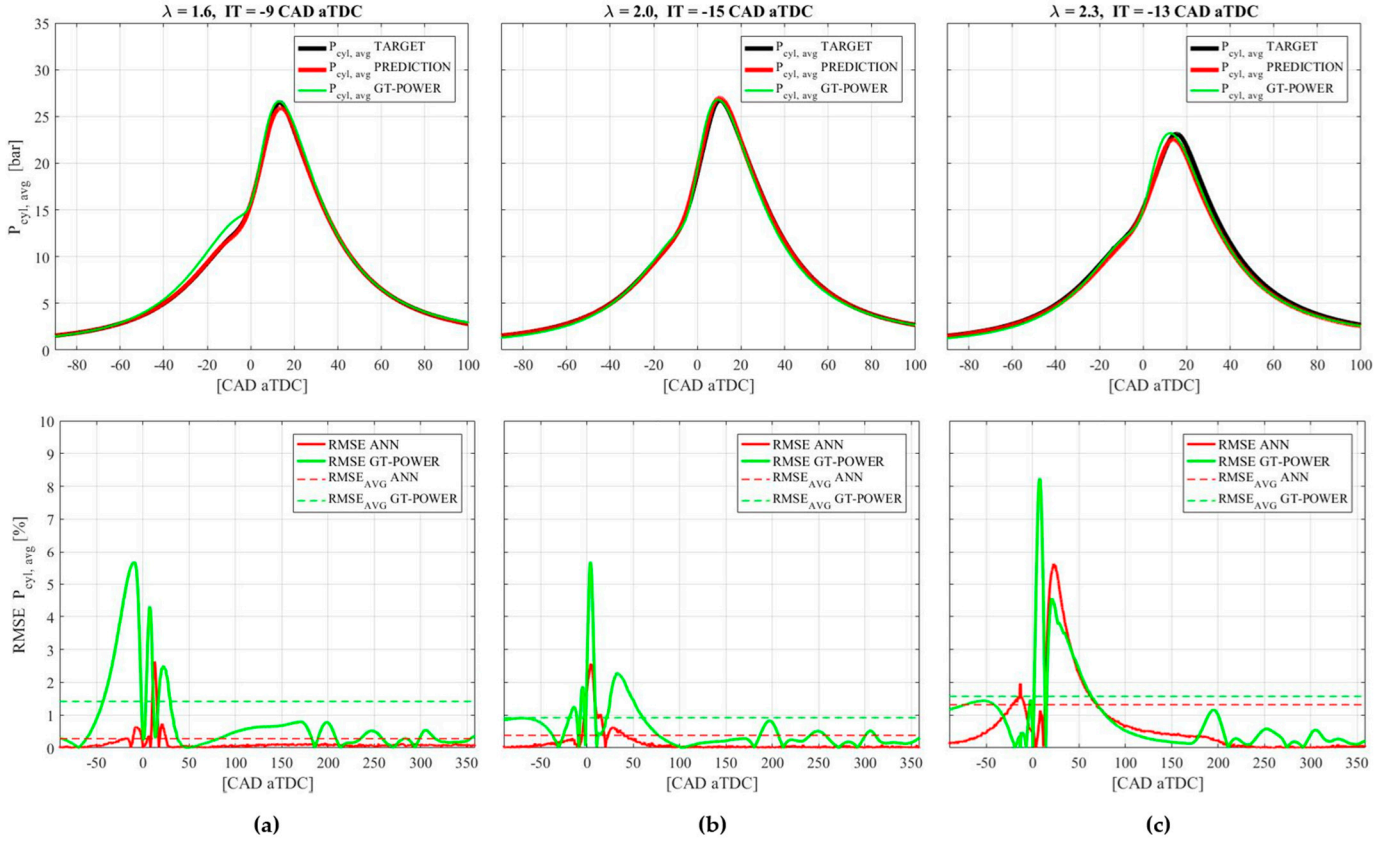



**Figure 13.** BPANN and GT-POWER $P_{cyl, avg}$ prediction performance for (**a**) $\lambda$ = 1.6 and IT = −9 CAD aTDC, (**b**) $\lambda$ = 2.0 and IT = −15 CAD aTDC, and (**c**) $\lambda$ = 2.3 and IT = −13 CAD aTDC.

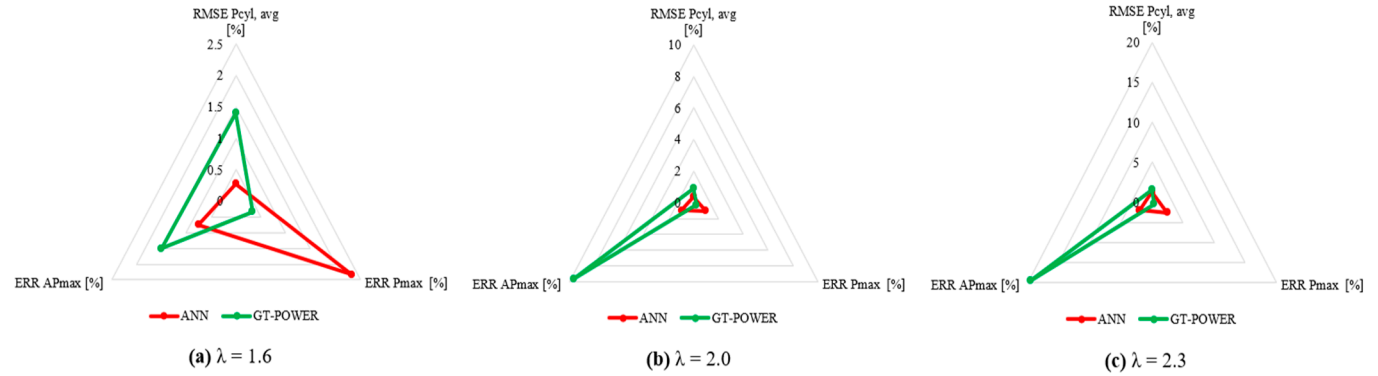



**Figure 14.** Radar charts which compare the prediction performance of BPANN and GT-POWER in terms of $P_{cyl, avg}$, ERR $P_{max}$, and ERR $AP_{max}$ for (**a**) $\lambda$ = 1.6, (**b**) $\lambda$ = 2.0, and (**c**) $\lambda$ = 2.3.

The ANN consistently achieves lower RMSE $P_{cyl, avg}$ values than GT-POWER across all $\lambda$ values. For example, at $\lambda$ = 1.6 (Figure 13a), ANN has an RMSE of 0.28%, while GT-POWER reaches 1.41%. This trend holds as $\lambda$ increases, with ANN maintaining lower RMSE values at $\lambda$ = 2.0 (Figure 13b) and 2.3 (Figure 13c). Furthermore, ANN's RMSE remains low and stable throughout the CAD range, while GT-POWER experiences significant fluctuations, particularly near TDC. Although GT-POWER shows slightly lower $P_{max}$ errors, ANN consistently performs better in predicting $AP_{max}$ with much lower errors, as shown in Figure 14 and Table 8. Importantly, ANN's ERR $P_{max}$ and ERR $AP_{max}$ values

consistently stay well below the 10% threshold, with a maximum error of 2.48% for $P_{max}$ and 1.96% for $AP_{max}$ (at $\lambda$ = 2.3), indicating high accuracy and stability. In contrast, GT-POWER's ERR $AP_{max}$ tends to approach and exceed this threshold (i.e., 9.62% at $\lambda$ = 2.0 and 19.61% at $\lambda$ = 2.3), making ANN more reliable and preferable for applications requiring precise in-cylinder pressure and timing predictions.

**Table 8.** Dataset 2: main results.

| $\lambda_{avg}$ [-] | RMSE $P_{cyl,\ avg}$ ANN [%] | RMSE $P_{cyl,\ avg}$ GT-POWER [%] | ERR $P_{max}$ ANN [%] | ERR $P_{max}$ GT-POWER [%] | ERR $AP_{max}$ ANN [%] | ERR $AP_{max}$ GT-POWER [%] |
|---|---|---|---|---|---|---|
| 1.6 | 0.28 | 1.41 | 2.33 | 0.33 | 0.75 | 1.50 |
| 2.0 | 0.38 | 0.92 | 0.99 | 0.25 | 0.96 | 9.62 |
| 2.3 | 1.32 | 1.57 | 2.48 | 0.35 | 1.96 | 19.61 |

### *4.3. Dataset 3 Results*

Figure 15 and Table 9 offer a comprehensive evaluation of the BPANN model's performance in predicting $P_{cyl}$ and $r_{eq}$ across multiple cycles within Dataset 3, as presented in Figure 8, with conditions of $\lambda$ = 1.6 and IT = −11 CAD aTDC. The primary metrics assessed include the RMSE for in-cylinder pressure and the RMSE for the equivalent flame radius (RMSE $r_{eq}$). The figure illustrates that, even in this case, the model accurately predicts the target values for both $P_{cyl}$ (Figure 15a) and $r_{eq}$ (Figure 15b), thereby demonstrating the model's robustness and accuracy under these operating conditions.

**Table 9.** Dataset 3: main results.

| Cycle Number [-] | RMSE $P_{cyl}$ [%] | RMSE $r_{eq}$ [%] |
|---|---|---|
| 1 | 0.25 | 2.21 |
| 2 | 0.52 | 2.26 |
| 3 | 0.32 | 2.87 |
| 4 | 0.30 | 2.79 |
| 5 | 0.36 | 2.21 |
| 6 | 0.40 | 2.67 |
| 7 | 0.45 | 2.40 |
| 8 | 0.47 | 2.78 |
| 9 | 0.25 | 2.90 |
| 10 | 0.38 | 2.43 |
| **avg.** | 0.37 | 2.55 |

As highlighted by the results presented earlier, the proposed model demonstrates effective convergence during the training process while successfully preventing overfitting. This capability highlights its effectiveness in extracting valuable insights from the dataset and attaining accurate predictions. The findings reveal that the ANN model not only surpasses GT-POWER in in-cylinder pressure prediction accuracy, achieving a minimum RMSE of 0.28% while never exceeding 2%, but also demonstrates a high level of predictive capability for the equivalent flame radius, with the associated RMSE consistently remaining below 4%. Moreover, the BP neural network exhibits substantial improvements in computational speed, highlighting its potential as a practical alternative for real-time diagnostics

and optimization. This underscores the emerging role of AI-based approaches in advancing hydrogen combustion technology, offering a path towards more sustainable and efficient automotive propulsion systems.

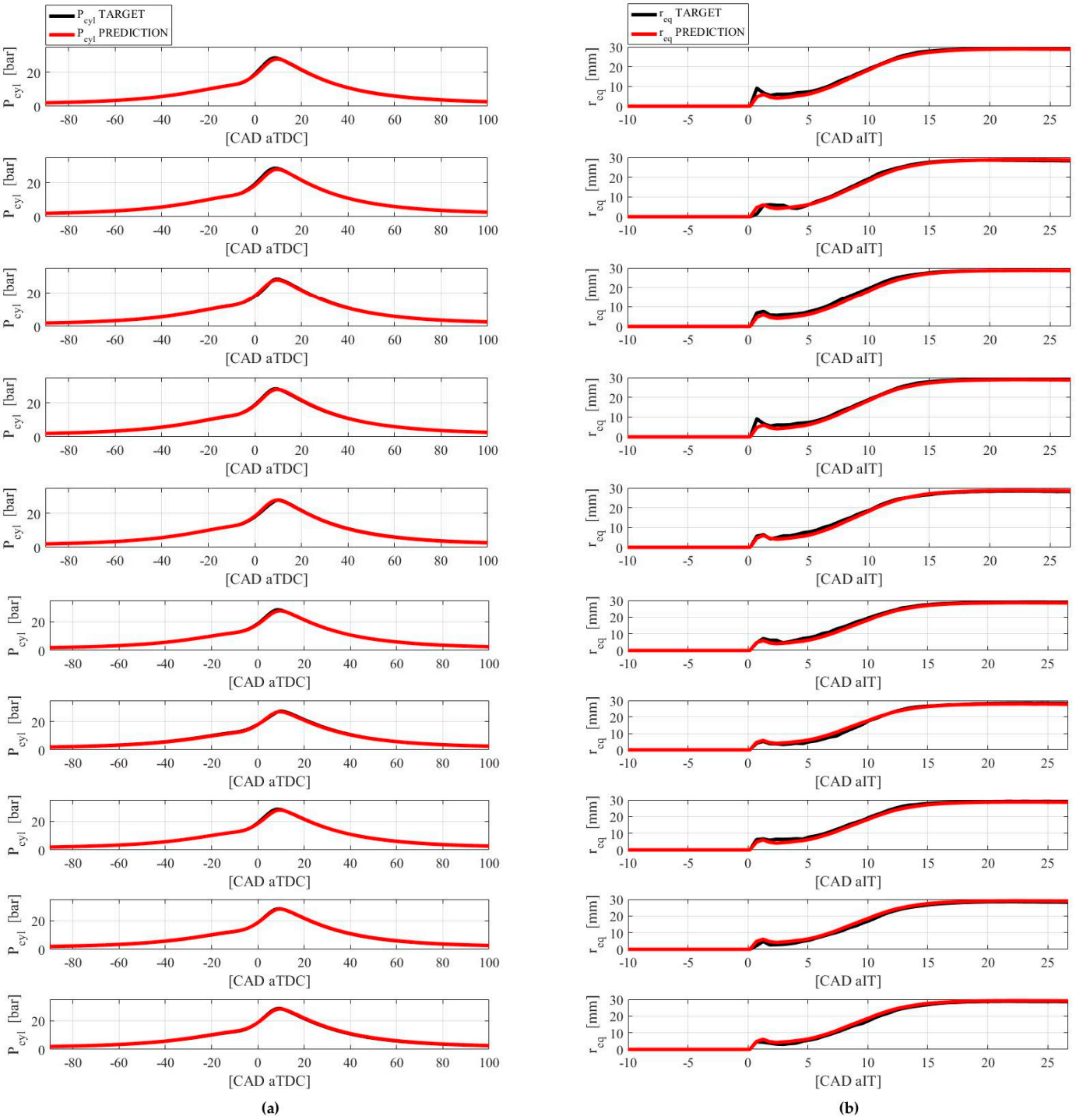



**Figure 15.** BPANN prediction of in-cylinder pressure (**a**) and equivalent flame radius (**b**) for $\lambda$ = 1.6 and IT = −11 CAD aTDC.

Moreover, regarding computational efficiency, it is important to note that both GT-POWER and the BPANN model were executed on the same computational platform, equipped with a single Central Processing Unit (CPU) and 16 GB of Random Access Memory (RAM). In GT-POWER, the simulation of a single operating case requires an average runtime of approximately 3 min, with peaks extending to 6/7 min. Furthermore,

achieving an efficient calibration of the model for each specific operating condition often necessitates multiple iterative attempts to refine its parameters. In contrast, while the BPANN model also underwent a calibration process involving the optimization of hidden layers, neurons, and activation functions, the training phase required approximately one minute, and the subsequent testing phase was virtually instantaneous. This highlights the superior computational efficiency of the BPANN model compared to the traditional GT-POWER approach.

## 5. Conclusions

This study demonstrates the effectiveness of artificial neural networks in predicting in-cylinder pressure and equivalent flame radius in hydrogen-fueled internal combustion engines. Comparative analyses with GT-POWER simulations reveal that the back propagation artificial neural network model achieves significantly greater predictive accuracy, with RMSE for in-cylinder pressure consistently below 0.44% across various conditions, compared to GT-POWER's RMSE range of 0.92% to 1.57%. The artificial neural network also accurately predicted maximum in-cylinder pressure and its corresponding crank angle, with error percentages for $P_{max}$ consistently under 2.5% and $AP_{max}$ errors well within a 10% threshold across all test conditions.

For the equivalent flame radius, the model maintained an RMSE of less than 3%, effectively modeling flame growth without relying on optical measurements. This capability underscores the practical value of the BPANN in predicting the equivalent flame radius, thereby eliminating the need for repeated testing with dedicated high-speed cameras in research engines with optical access, due to the significant resources required for data acquisition and post-processing. Moreover, this approach can potentially be applied to conventional road engines exhibiting characteristics and performance similar to those of a specific optical engine used in the machine learning analysis.

Furthermore, the GT-POWER model setup and calibration proved to be both time-consuming and resource-intensive, as they required detailed technical specifications of engine parameters, including geometries, fluid conditions, and precise combustion boundary definitions. These extensive requirements translate to long setup times and a need for substantial computational resources, which limits the feasibility of GT-POWER for real-time applications. The BPANN model, by providing accurate predictions and computational efficiency with minimal setup and training time, offers a more streamlined alternative for real-time engine diagnostics.

Overall, these findings underscore the BPANN's viability as an advanced diagnostic tool, achieving a minimum RMSE $P_{cyl}$ of 0.28% and maintaining the $AP_{max}$ error below 2% at critical operating points. These advancements mark a step toward integrating machine learning technologies in hydrogen combustion systems, enhancing predictive accuracy and efficiency for sustainable automotive propulsion.

**Author Contributions:** Conceptualization, F.R. and F.M.; methodology, F.R. and M.A.; software, F.R. and M.A.; validation, F.M.; formal analysis, F.R. and M.A.; investigation, F.R. and M.A.; resources, F.M.; data curation, F.R. and M.A.; writing—original draft preparation, F.R. and M.A.; writing—review and editing, F.R., M.A. and F.M.; visualization, F.R. and M.A.; supervision, F.M.; project administration, F.M. All authors have read and agreed to the published version of the manuscript.

**Funding:** This research received no external funding.

**Institutional Review Board Statement:** Not applicable.

**Informed Consent Statement:** Not applicable.

**Data Availability Statement:** Dataset available on request from the authors.

**Conflicts of Interest:** The authors declare no conflicts of interest.

## Nomenclature

| | |
|---|---|
| AI | artificial intelligence |
| ANN | artificial neural network |
| $AP_{max}$ | crank angle degree at which $P_{max}$ occurs |
| aBDC | after bottoming dead center |
| aIT | after ignition timing |
| aTDC | after top dead center |
| BP | back-propagation |
| BPANN | back-propagation artificial neural network |
| CAD | crank angle degree |
| CFD | computational fluid dynamics |
| CPU | central processing unit |
| E85 | ethanol |
| ECU | engine control unit |
| ERR | percentage error |
| FFNN | feed-forward neural network |
| FL | fuzzy logic |
| GHG | greenhouse gasses |
| $H_2$ | hydrogen |
| ICE | internal combustion engine |
| IMEP | indicated mean effective pressure |
| IT | ignition timing |
| $\lambda(1/\varphi)$ | air excess coefficient |
| M100 | methanol |
| MAE | mean absolute error |
| MBT | maximum brake torque |
| MFB | mass fraction burned |
| ML | machine learning |
| MSE | mean squared error |
| $NO_x$ | nitrogen oxides |
| $O_2$ | oxygen |
| $P_{cyl}$ | in-cylinder pressure |
| $P_{cyl,\,avg}$ | average value of the in-cylinder pressure |
| $P_{max}$ | maximum in-cylinder pressure |
| PFI | port fuel injection |
| $R^2$ | coefficient of determination |
| $r_{eq}$ | equivalent flame radius |
| RAM | random access memory |
| RBF | radial basis function |
| RMSE | root mean square error |
| TVO | throttle valve opening |

## References

1. Joshi, A. Review of vehicle engine efficiency and emissions. *SAE Int. J. Adv. Curr. Pract. Mobil.* **2020**, *2*, 2479–2507. [CrossRef]
2. Wallington, T.J.; Anderson, J.E.; Dolan, R.H.; Winkler, S.L. Vehicle emissions and urban air quality: 60 years of progress. *Atmosphere* **2022**, *13*, 650. [CrossRef]
3. Berggren, C.; Magnusson, T. Reducing automotive emissions—The potentials of combustion engine technologies and the power policy. *Energy Policy* **2012**, *41*, 636–643. [CrossRef]
4. Shahzad, K.; Cheema, I.I. Low-carbon technologies in automotive industry and decarbonizing transport. *J. Power Sources* **2024**, *591*, 233888. [CrossRef]

5. Reitz, R.D.; Ogawa, H.; Payri, R.; Fansler, T.; Kokjohn, S.; Moriyoshi, Y.; Agarwal, A.; Arcoumanis, D.; Assanis, D.; Bae, C.; et al. IJER editorial: The future of the internal combustion engine. *Int. J. Engine Res.* **2020**, *21*, 3–10. [CrossRef]
6. Kalghatgi, G.; Johansson, B. Gasoline compression ignition approach to efficient, clean and affordable future engines. *Proc. Inst. Mech. Eng. Part D J. Automob. Eng.* **2018**, *232*, 118–138. [CrossRef]
7. Ehsani, M.; Singh, K.V.; Bansal, H.O.; Mehrjardi, R.T. State of the Art and Trends in Electric and Hybrid Electric Vehicles. *Proc. IEEE* **2021**, *109*, 967–984. [CrossRef]
8. Pielecha, J.; Skobiej, K.; Kurtyka, K. Exhaust emissions and energy consumption analysis of conventional, hybrid, and electric vehicles in real driving cycles. *Energies* **2020**, *13*, 6423. [CrossRef]
9. Anika, O.C.; Nnabuife, S.G.; Bello, A.; Okoroafor, E.R.; Kuang, B.; Villa, R. Prospects of low and zero-carbon renewable fuels in 1.5-degree net zero emission actualization by 2050: A critical review. *Carbon Capture Sci. Technol.* **2022**, *5*, 100072. [CrossRef]
10. Baldinelli, A.; Francesconi, M.; Antonelli, M. Hydrogen, E-Fuels, Biofuels: What Is the Most Viable Alternative to Diesel for Heavy-Duty Internal Combustion Engine Vehicles? *Energies* **2024**, *17*, 4728. [CrossRef]
11. Ricci, F.; Mariani, F.; Papi, S.; Zembi, J.; Battistoni, M.; Grimaldi, C.N. The Synergy between Methanol M100 and Plasma-Assisted Ignition System PAI to Achieve Increasingly Leaner Mixtures in a Single-Cylinder Engine. *Energies* **2024**, *17*, 1659. [CrossRef]
12. Martinelli, R.; Ricci, F.; Zembi, J.; Battistoni, M.; Grimaldi, C.; Papi, S. *Lean Combustion Analysis of a Plasma-Assisted Ignition System in a Single Cylinder Engine Fueled with E85*; SAE Technical Paper 2022-24-0034; SAE International: Warrendale, PA, USA, 2022.
13. Falfari, S.; Cazzoli, G.; Mariani, V.; Bianchi, G.M. Hydrogen Application as a Fuel in Internal Combustion Engines. *Energies* **2023**, *16*, 2545. [CrossRef]
14. Onorati, A.; Payri, R.; Vaglieco, B.; Agarwal, A.; Bae, C.; Bruneaux, G.; Canakci, M.; Gavaises, M.; Gunthner, M.; Hasse, C.; et al. The role of hydrogen for future internal combustion engines. *Int. J. Engine Res.* **2022**, *23*, 529–540. [CrossRef]
15. Duan, X.; Xu, L.; Xu, L.; Jiang, P.; Gan, T.; Liu, H.; Ye, S.; Sun, Z. Performance analysis and comparison of the spark ignition engine fueled with industrial by-product hydrogen and gasoline. *J. Clean. Prod.* **2023**, *424*, 138899. [CrossRef]
16. Sementa, P.; Antolini, J.B.d.V.; Tornatore, C.; Catapano, F.; Vaglieco, B.M.; Sánchez, J.J.L. Exploring the potentials of lean-burn hydrogen SI engine compared to methane operation. *Int. J. Hydrogen Energy* **2022**, *47*, 25044–25056. [CrossRef]
17. Avana, M.; Ricci, F.; Papi, S.; Zembi, J.; Battistoni, M.; Grimaldi, C.N. *Performance Analysis of Hydrogen Combustion Under Ultra Lean Conditions in a Spark Ignition Research Engine Using a Barrier Discharge Igniter*; SAE Technical Paper 2024-24-0036; SAE International: Warrendale, PA, USA, 2024.
18. Du, H.; Chai, W.S.; Wei, H.; Zhou, L. Status and challenges for realizing low emission with hydrogen ultra-lean combustion. *Int. J. Hydrogen Energy* **2024**, *57*, 1419–1436. [CrossRef]
19. Aydin, K.; Kutanoglu, R. Effects of hydrogenation of fossil fuels with hydrogen and hydroxy gas on performance and emissions of internal combustion engines. *Int. J. Hydrogen Energy* **2018**, *43*, 14047–14058. [CrossRef]
20. Shi, C.; Ji, C.; Wang, S.; Yang, J.; Wang, H. Experimental and numerical study of combustion and emissions performance in a hydrogen-enriched Wankel engine at stoichiometric and lean operations. *Fuel* **2021**, *291*, 120181. [CrossRef]
21. Ricci, F.; Zembi, J.; Avana, M.; Grimaldi, C.N.; Battistoni, M.; Papi, S. Analysis of Hydrogen Combustion in a Spark Ignition Research Engine with a Barrier Discharge Igniter. *Energies* **2024**, *17*, 1739. [CrossRef]
22. Suresh, D.; Porpatham, E. Influence of high compression ratio and hydrogen addition on the performance and emissions of a lean burn spark ignition engine fueled by ethanol-gasoline. *Int. J. Hydrogen Energy* **2023**, *48*, 14433–14448. [CrossRef]
23. Diéguez, P.M.; Urroz, J.; Sáinz, D.; Machin, J.; Arana, M.; Gandía, L. Characterization of combustion anomalies in a hydrogen fueled 1.4 L commercial spark-ignition engine by means of in-cylinder pressure, block-engine vibration, and acoustic measurements. *Energy Convers. Manag.* **2018**, *172*, 67–80. [CrossRef]
24. Gao, J.; Wang, X.; Song, P.; Tian, G.; Ma, C. Review of the backfire occurrences and control strategies for port hydrogen injection internal combustion engines. *Fuel* **2022**, *307*, 121553. [CrossRef]
25. Gao, J.; Yao, A.; Zhang, Y.; Qu, G.; Yao, C.; Zhang, S.; Li, D. Investigation into the relationship between super-knock and misfires in an SI GDI engine. *Energies* **2021**, *14*, 2099. [CrossRef]
26. Yang, Z.; Wu, J.; Yun, H.; Zhang, H.; Xu, J. Diagnosis and control of abnormal combustion of hydrogen internal combustion engine based on the hydrogen injection parameters. *Int. J. Hydrogen Energy* **2022**, *47*, 15887–15895. [CrossRef]
27. Ye, Y.; Gao, W.; Li, Y.; Zhang, P.; Cao, X. Numerical study of the effect of injection timing on the knock combustion in a direct-injection hydrogen engine. *Int. J. Hydrogen Energy* **2020**, *45*, 27904–27919. [CrossRef]
28. Verhelst, S.; Demuynck, J.; Sierens, E.; Huyskens, P. Impact of variable valve timing on power, emissions and backfire of a bi-fuel hydrogen/gasoline engine. *Int. J. Hydrogen Energy* **2010**, *35*, 4399–4408. [CrossRef]
29. Srinivasan, C.B.; Subramanian, R. Hydrogen as a Spark Ignition Engine Fuel Technical Review. *Int. J. Mech. Mechatron. Eng. IJMME-IJENS* **2014**, *14*, 111–117.
30. Wang, Y. A novel two-zone thermodynamic model for spark-ignition engines based on an idealized thermodynamic process. *Energies* **2020**, *13*, 3801. [CrossRef]

31. Corrigan, D.J.; Breda, S.; Fontanesi, S. *A Simple CFD Model for Knocking Cylinder Pressure Data Interpretation: Part 1*; SAE Technical Paper 2021-24-0051; SAE International: Warrendale, PA, USA, 2021.
32. Sizikov, V.S.; Sidorov, D.N. Generalized quadrature for solving singular integral equations of Abel type in application to infrared tomography. *Appl. Numer. Math.* **2016**, *106*, 69–78. [CrossRef]
33. Sun, Y.; Lv, L.; Lee, P.; Cai, Y. Prediction of in-cylinder pressure of diesel engine based on extreme gradient boosting and sparrow search algorithm. *Appl. Sci.* **2022**, *12*, 1756. [CrossRef]
34. Maroteaux, F.; Sebai, S.; Mancaruso, E.; Rossetti, S.; Schembri, P.; Radja, K.; Barichella, A. *Numerical and Experimental Analysis of Dual Fuel Hydrogen/Diesel Combustion at Varying Engine Speed on a Single Cylinder Engine*; SAE Technical Paper 2024-24-0044; SAE International: Warrendale, PA, USA, 2024.
35. Bakar, R.A.; Mohammed, M.K.; Rahman, M.M. Numerical study on the performance characteristics of hydrogen fueled port injection internal combustion engine. *Am. J. Eng. Appl. Sci* **2009**, *2*, 407–415. [CrossRef]
36. Kulkarni, D.; Patil, A.; Wagh, J.; Chougule, S.D. Modelling of Internal Combustion Engine using GT Power. *Int. J. Eng. Res. Technol. (IJERT)* **2019**, *8*, 92–94.
37. Done, L.; Lahane, S.; Nandgaonkar, M.R. Modeling of Single Cylinder Compression Ignition Engine by Using GT-Power Software and Performance Analysis. In Proceedings of the 2nd Indian International Conference on Industrial Engineering and Operations Management Warangal, Telangana, India, 16–18 August 2022.
38. Zhao, F.; Hung, D.L.S. Applications of machine learning to the analysis of engine in-cylinder flow and thermal process: A review and outlook. *Appl. Therm. Eng.* **2023**, *220*, 119633. [CrossRef]
39. Fang, L.; Singh, H.; Ohashi, T.; Sanno, M.; Lin, G.; Yilmaz, E.; Ichiyanagi, M.; Suzuki, T. Effect of Machine Learning Algorithms on Prediction of In-Cylinder Combustion Pressure of Ammonia–Oxygen in a Constant-Volume Combustion Chamber. *Energies* **2024**, *17*, 746. [CrossRef]
40. Ricci, F.; Avana, M.; Mariani, F. Enhancing Lambda Measurement in Hydrogen-Fueled SI Engines through Virtual Sensor Implementation. *Energies* **2024**, *17*, 3932. [CrossRef]
41. Hanuschkin, A.; Schober, S.; Bode, J.; Schorr, J.; Böhm, B.; Krüger, C.; Peters, S. Machine learning–based analysis of in-cylinder flow fields to predict combustion engine performance. *Int. J. Engine Res.* **2021**, *22*, 257–272. [CrossRef]
42. Solmaz, Ö.; Gürbüz, H.; Karacor, M. Comparison of artificial neural network and fuzzy logic approaches for the prediction of in-cylinder pressure in a spark ignition engine. *J. Dyn. Syst. Meas. Control* **2020**, *142*, 091005. [CrossRef]
43. Bizon, K.; Continillo, G.; Lombardi, S.; Mancaruso, E.; Vaglieco, B.M. ANN-based virtual sensor for on-line prediction of in-cylinder pressure in a diesel engine. *Comput. Aided Chem. Eng.* **2014**, *33*, 763–768.
44. Murugesan, S.; Srihari, S.; Senthilkumar, D. *Investigation of Usage of Artificial Neural Network Algorithms for Prediction of In-Cylinder Pressure in Direct Injection Engines*; SAE Technical Paper 2022-01-5089; SAE International: Warrendale, PA, USA, 2022.
45. Wright, L.G.; Onodera, T.; Stein, M.M.; Wang, T.; Schachter, D.T.; Hu, Z.; McMahon, P.L. Deep physical neural networks trained with backpropagation. *Nature* **2022**, *601*, 549–555. [CrossRef]
46. Irimescu, A.; Tornatore, C.; Marchitto, L.; Merola, S.S. Compression Ratio and Blow-by Rates Estimation Based on Motored Pressure Trace Analysis for an Optical Spark Ignition Engine. *Appl. Therm. Eng.* **2013**, *61*, 101–109. [CrossRef]
47. Merola, S.S.; Irimescu, A.; Tornatore, C.; Valentino, G. Effect of the Fuel-Injection Strategy on Flame-Front Evolution in an Optical Wall-Guided DISI Engine with Gasoline and Butanol Fueling. *J. Energy Eng.* **2016**, *142*, E4015004. [CrossRef]
48. Azeem, N.; Beatrice, C.; Vassallo, A.; Pesce, F.; Davide, G.; Guido, C. *Comparative Analysis of Different Methodologies to Calculate Lambda (λ) Based on Extensive and systemic Experimentation on a Hydrogen Internal Combustion Engine*; SAE Technical Paper 2023-01-0340; SAE International: Warrendale, PA, USA, 2023.
49. Cruccolini, V.; Discepoli, G.; Ricci, F.; Petrucci, L.; Grimaldi, C.; Papi, S.; Dal Re, M. *Comparative Analysis Between a Barrier Discharge Igniter and a Streamer-Type Radio-Frequency Corona Igniter in an Optically Accessible Engine in Lean Operating Conditions*; SAE Technical Paper 2020-01-0276; SAE International: Warrendale, PA, USA, 2020.
50. Ricci, F.; Mariani, F. Advanced Flame front Detection in Combustion Processes Using Autoencoder Approach. *Energies* **2024**, *17*, 1759. [CrossRef]
51. Shawal, S.; Goschutz, M.; Schild, M.; Kaiser, S.; Neurohr, M.; Pfeil, J.; Koch, T. High-speed imaging of early flame growth in spark-ignited engines using different imaging systems via endoscopic and full optical access. *SAE Int. J. Engines* **2016**, *9*, 704–718. [CrossRef]
52. Aleiferis, P.G.; Serras-Pereira, J.; Richardson, D. Characterization of flame development with ethanol, butanol, iso-octane, gasoline and methane in a direct-injection spark-ignition engine. *Fuel* **2013**, *109*, 256–278. [CrossRef]
53. GT-POWER: Engine Performance Application Manual; Gamma Technologies LLC 2024. Available online: https://www.gtisoft.com/gt-power/ (accessed on 11 November 2024).
54. GT-SUITE: Integrated Multiphysics Systems Simulation; Gamma Technologies LLC 2024. Available online: https://www.gtisoft.com/gt-suite/ (accessed on 11 November 2024).

55. Choi, S.; Kolodziej, C.P.; Hoth, A.; Wallner, T. *Development and Validation of a Three-Pressure Analysis (tpa) gt-Power Model of the cfr f1/f2 Engine for Estimating Cylinder Conditions*; SAE Technical Paper 2018-01-0848; SAE International: Warrendale, PA, USA, 2018.
56. Singh, A.; Kushwaha, S.; Alarfaj, M.; Singh, M. Comprehensive overview of backpropagation algorithm for digital image denoising. *Electronics* **2022**, *11*, 1590. [CrossRef]
57. Cui, Y.; Liu, H.; Wang, Q.; Zheng, Z.; Wang, H.; Yue, Z.; Ming, Z.; Wen, M.; Feng, L.; Yao, M. Investigation on the ignition delay prediction model of multi-component surrogates based on back propagation (BP) neural network. *Combust. Flame* **2022**, *237*, 111852. [CrossRef]
58. Ricci, F.; Avana, M.; Mariani, F. A Deep Learning Method for the Prediction of Pollutant Emissions from Internal Combustion Engines. *Appl. Sci.* **2024**, *14*, 9707. [CrossRef]

**Disclaimer/Publisher's Note:** The statements, opinions and data contained in all publications are solely those of the individual author(s) and contributor(s) and not of MDPI and/or the editor(s). MDPI and/or the editor(s) disclaim responsibility for any injury to people or property resulting from any ideas, methods, instructions or products referred to in the content.